Progress in Additive Manufacturing (2026) 11:2285–2294
https://doi.org/10.1007/s40964-025-01467-w

RESEARCH

Controlling microstructure formation in metal additive manufacturing via deep learning driven spatiotemporal temperature regulation

Fan Wu[1] · Clint Grohmann[1,2] · Feng Ji[3] · Zhe Cai[1] · Lu Yang[1] · Paulo Bartolo[3,4] · Wajira Mirihanage[1]

Received: 8 June 2025 / Accepted: 3 December 2025 / Published online: 8 January 2026

Abstract

Microstructure control and high residual stresses remain key challenges in metal additive manufacturing. A novel artificial intelligence-based framework, which considers the underpinning thermal evolution, was developed to generate laser scanning strategies that can mitigate these issues. The framework integrates a convolutional neural network (CNN) and a genetic algorithm (GA): the CNN predicts temporal and spatial temperature distributions, while the GA optimizes laser scanning sequences based on designated criteria. To validate the approach, laser scanning strategies for laser powder bed fusion of stainless steel 316 L were generated and experimentally implemented. The scanning pattern designed to maximize cooling rate produced refined microstructures. Similarly, microstructure characterization revealed reduced kernel average misorientation values in samples fabricated using the minimised temperature gradient criterion, indicating lower residual stress and local plastic strain. This preliminary experimental validation demonstrates the potential of this solidification conditions associated with deep learning based framework to control microstructure and defect formation in metal additive manufacturing, particularly for larger and more realistic component sizes.

Keywords Artificial intelligence · Electron backscatter diffraction (EBSD) · Laser powder bed fusion · Scanning strategy

Fan Wu and Clint Grohmann are co-first authors.

✉ Fan Wu
fan.wu-6@manchester.ac.uk

✉ Wajira Mirihanage
wajira.mirihanage@manchester.ac.uk

Clint Grohmann
clint.grohmann@materials.ox.ac.uk

Feng Ji
crystal.ji@ntu.edu.sg

Zhe Cai
zhe.cai-2@manchester.ac.uk

Lu Yang
lu.yang@manchester.ac.uk

Paulo Bartolo
pbartolo@ntu.edu.sg

[1] The University of Manchester, Manchester, UK M13 9PL

[2] Department of Materials, University of Oxford, Oxford OX1 3PH, UK

[3] Mechanical & Aerospace Engineering, Nanyang Technological University, Singapore, Singapore

[4] Singapore Centre for 3D Printing, Singapore, Singapore

1 Introduction

Metal additive manufacturing (AM) offers the promising ability to build complex components. Laser powder bed fusion (LPBF) is a widely adopted metal AM method across different industries [1, 2]. The scanning strategies employed to build individual layers of materials in the LPBF and other AM processes directly influence the thermal evolution during manufacturing, including temperature gradients and cooling rates [3, 4]. Conventional scanning strategies often result in localised heat accumulation and steep thermal gradients [5–8]. These thermal demerits lead to defective manufacturing quality such as undesirable microstructures and residual stresses [9–11].

Considerable experimental [12–16] and simulation [8, 17–19] efforts have been dedicated to investigating the effects of various scanning strategies on the AM components. Liu et al. [15] introduced adding non-laser scanning segments after scan lines to maintain consistent scan line lengths, effectively reducing overheating accumulation. This approach lowered peak temperatures and minimised porosity and other defects. Nadammal et al. [20] investigated

the use of unconventional scanning strategies, such as the alternating and rotational scanning strategies. They demonstrated that precise control of scanning strategies could effectively modify the microstructure and residual stresses distribution in LPBF manufactured parts. Through modelling, Evans et al. [21] evaluated different scan path lengths for varying sample thicknesses to control the final structure. Experiments also demonstrated that shorter scanning vectors can reduce residual stress [22, 23]. Consequently, island scanning strategies that divide each layer into islands forming a checkerboard pattern, with each island raster-scanned using shorter scan tracks, effectively reduce residual stress and cracking during manufacturing [13, 18, 24–26].

Optimising scanning strategies requires testing many sequences. Such testing is limited by resource and time constraints, making it impractical to conduct extensive testing either experimentally or through numerical simulations. Machine learning (ML) approaches have emerged as a prospective tool for optimising AM scanning strategies. It can process vast and complex datasets to uncover patterns that conventional methods might overlook, offering faster training and more efficient predictions compared to physics-based simulations. Recent studies [27–32] have begun to explore the potential of ML methods for improving scanning strategies and final part quality in AM processes. Qin et al. [27] utilised deep reinforcement learning to optimise scanning path generation in LPBF process. This approach achieved uniform thermal distribution and minimised residual stress in stainless steel components 316L (SS316L). Dharmawan et al. [30] used reinforcement learning to enhance surface quality and shape accuracy in wire arc additive manufacturing of bronze and stainless steel. ML methods to optimise AM parameters like laser power and scanning speed also were reported [33].

Although ML and artificial intelligence (AI) have been increasingly applied to optimise additive manufacturing processes, several limitations persist. Most existing studies focus on parameter level optimisation, such as tuning laser power or scanning speed, which fails to capture the spatiotemporal heat evolution that governs microstructure formation and residual stress development. In addition, existing frameworks rarely integrate artificial intelligence, in particularly deep learning based temperature field design/prediction with evolutionary optimisation algorithms, leaving the link between thermal field estimation and scanning strategy design incomplete. Experimental validation is also limited, with many approaches remaining at the simulation level or assessing only macroscopic build quality rather than microstructural characteristics.

To address these limitations, the present work introduces a comprehensive AI framework that directly regulates the spatiotemporal temperature field during metal additive manufacturing. The proposed approach combines a convolutional neural network (CNN) for predicting thermal evolution with a genetic algorithm (GA) for optimising island printing sequences. The CNN rapidly predicts the spatiotemporal evolution of the temperature field, while the GA performs global optimisation to determine the optimal scanning sequence that regulates cooling rates and temperature gradients. This combination provides a physics informed and computationally efficient route to control heat accumulation and cooling rate, which achieve microstructural refinement and make an advancement beyond existing data-driven or parameter-optimisation approaches. The effectiveness of the CNN-GA framework is validated experimentally using laser powder bed fusion (LPBF) of stainless steel 316L, demonstrating its ability to tailor microstructural features according to specific metallurgical objectives such as grain refinement.

2 Deep learning pipeline

The proposed approach incorporates physical modelling and deep learning. The overall mechanism was constructed on the physical basis for thermal evolution, followed by algorithmic optimisation of the island printing sequence. The optimisation of island printing strategies for achieving refined microstructure and reduced residual stresses were considered in this preamble study.

An iterative model based on the 2D heat equation was employed to estimate spatiotemporal evolution of temperature during the additive process, as described [34]:

$$\alpha \left(\frac{\partial^2 T}{\partial x^2} + \frac{\partial^2 T}{\partial y^2} \right) = \frac{\partial T}{\partial t} \tag{1}$$

where T is temperature, t is time, α is thermal diffusivity and x and y are spatial dimensions. For this model, the thermal diffusivity of solidified metal and unfused powder is considered different. SS316L is studied for the predictive demonstrations, α was set as $0.35 \times 10^{-5}\,\mathrm{m^2 s^{-1}}$ for solidified Sect [35]. , while unfused powder was assumed to have one-tenth that. The domain was discretised into 1 mm spatial intervals corresponding to island size, with the time of printing an island taken as 0.0142 s from machine parameters. This is done since isothermal internal temperature distribution within each single island is considered and thus assumed to be negligeable for the purpose of optimisation of the gradient calculation between the islands. To enable efficient generation of a large training dataset (10,000 data points), the model incorporated simplifying assumptions, including disregarding convection and assuming the powder bed acts as an infinite heat sink. Each training data point contained

initial and final thermal distributions after laser passes, with heat transfer efficiency assumed to be 8%. Random thermal histories were also generated and included to enable learning of more complex scenarios where islands may have varied fusion states (more details of the finite difference method (FDM) employed can be found in supplementary information, see annex A).

Subsequently, two fitness evaluation algorithms (maximised cooling rate for finer grains and minimised thermal gradient for reduced residual stress) were developed to assess island printing strategies. The first algorithm evaluated cooling rate fitness by measuring temperature decrease for an island during the printing of subsequent islands, which directly influences grain size, as described by;

$$\dot{T} = \frac{d_T}{d_t} \tag{2}$$

where $\dot{T}$ represents the cooling rate, d_T represents the temperature change, and d_t represents corresponding time duration. The second algorithm assessed residual stress potential based on the thermal expansion relationship [36]:

$\frac{\Delta L}{L_0} = \alpha \Delta T$ (3) $\Delta T = \frac{d_T}{d_x}$ (4).

where ΔL is the expansion or contraction, L_0 is the original length, α is the thermal expansion coefficient, ΔT is the thermal gradient and d_x represents the spatial position change. To minimize residual stresses, mean thermal gradients across the sample were calculated using Eq. (4), and the thermal gradient cost was evaluated using Eq. (6). It should be noted that this assessment produces a cost rather than a fitness value, as the objective is minimisation. Both algorithms utilised spatial, and temporal resolved temperature data derived from proposed printing strategies.

To implement the optimisation process, two learning approaches were utilised, as shown in Fig. 1a. First, a CNN was trained to efficiently approximate thermal distributions by mimicking the 2D heat Eqs [37, 38]. The training data comprised three input arrays: initial thermal distribution, the next island to be printed, and all previously fused islands. The CNN architecture consisted of three residual neural network (ResNet) layers, each containing 64 padded convolutional kernels (3 × 3 dimension) with batch normalisation and rectified linear unit (ReLU) activation [39], achieving a mean squared error of approximately 10^{-2} K compared to iteratively estimated training heat data. This implementation utilised the Keras TensorFlow library [40]. Second, a custom genetic algorithm was employed to optimise printing sequences by switching the order of islands printed rather than altering conventional parameters. The evaluation process was accelerated through parallelisation

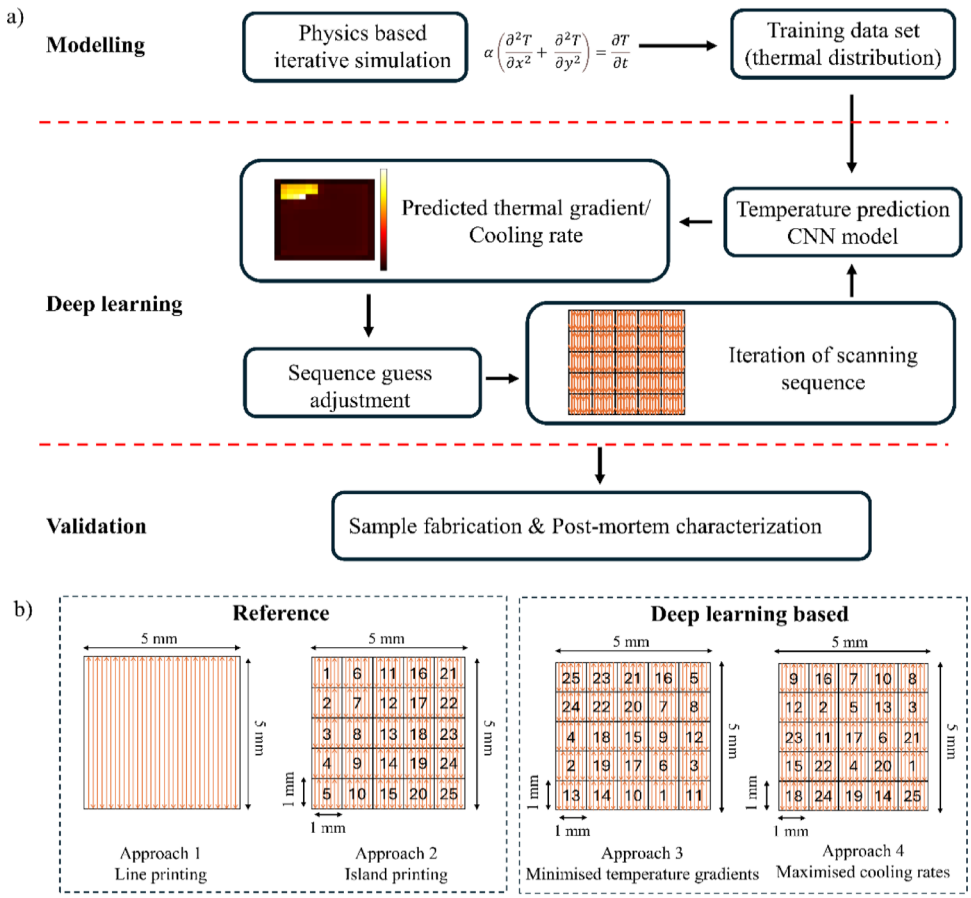

Fig. 1 **a** Overview of the deep learning-assisted scanning strategy optimisation pipeline. **b** Scanning strategies comparing two conventional reference approaches and two deep learning-based approaches

of fitness assessment using the trained CNN. Each generation consisted of 64 printing sequences, with the best-performing individual carried forward to the next generation along with 32 variations with different mutation degrees, where mutations are a switch of randomly selected parts of the sequence. This combined approach ultimately led to two optimised island printing sequences: one that maximised cooling rates to minimise grain size, and another that minimised temperature gradients to reduce residual stresses.

Using the computational methodology described above, fitness and cost functions based on metallurgical criteria were implemented into the genetic algorithm. A cooling rate fitness was calculated as;

$$F_{\dot{T}} = T_{ij_{n-1}} - T_{ij_n} \tag{5}$$

where *ij* is the location printed in timestep *n-1*.

In addition, thermal gradient cost was defined as;

$$C_G = \frac{\sum_{i=0,j=0}^{5} \left(\frac{|T_{ij}-T_{ij-1}|+|T_{ij}-T_{ij+1}|+|T_{ij}-T_{i-1j}|+|T_{ij}-T_{i+1j}|}{4} \right)}{n} \tag{6}$$

where C_G is the dimensionless thermal gradient cost parameter, T_{ij} represents the temperature value at grid position (i, j), and *n* denotes the total number of islands within the computational domain, where $n = 25$ for all approaches tested in this study.

3 Experimental

Four LPBF-AM scanning approaches were experimentally evaluated with SS316L. The first two (reference) approaches included line printing with dimensions of 5×5 mm^2 and conventional island printing composed of 25 independent islands (each 1×1 mm^2) with overall dimensions of 5×5 mm^2. The geometry and the sample size was selected to keep a balance between computational efficiency and experimental feasibility. This dimension enables efficient simulation and deep learning training. It also provides an appropriate area for post-process characterisation such as electron backscatter diffraction (EBSD). Additionally, two deep learning-based scanning approaches (minimised temperature gradients and maximised cooling rates) were implemented with dimensions identical to the conventional island printing approach, differing only in their scanning strategies (see Fig. 1b).

To fabricate the test samples, gas atomised SS316L powder with a particle size distribution of 20–65 µm was used (see supplementary Fig. S1). EOS® M290 LPBF system was employed for sample fabrication and the system was fitted with an Yttrium fibre laser with 1060–1100 nm wavelength. The diameter of the focused beam was approximately 0.1 mm. Argon was supplied to maintain the inert environment with an average flow rate of approximately 0.6 m^3/h. All the samples were processed with 250 W laser power, 1000 mm/s scanning speed, and 0.07 mm hatch spacing. The layer thickness was maintained at 0.035 mm. All design files were prepared using SolidWorks® and EOS® Print software. These parameters were kept constant for all island-scanning strategies and line printing to ensure that variations in the results originate solely from differences in scanning sequence design rather than from changes in process parameters.

Post-process characterisation was conducted on the as-built specimens using a Tescan® LC scanning electron microscope. An Oxford Instruments® EBSD detector was equipped to examine the grain size and internal state to evaluate stress conditions. Five representative areas (500 µm × 500 µm) were selected for EBSD indexing from the four corners and the centre of the specimens, as shown in Fig. S2. Using AZtec Crystal® software, EBSD results were processed to extract grain size and kernel average misorientation (KAM).

4 Results and discussion

4.1 Deep learning derived thermal gradient

The simulated mean absolute thermal gradient at a printed island for different scanning strategies including, minimised temperature gradient, maximised cooling rate and reference island printing are shown in Fig. 2a. The trend lines illustrate the overall evolution of thermal gradient during the additive process of each strategy. As shown in the figure, conventional scanning strategy tends to produce higher thermal gradients in the early stages and potentially leading to residual stress issues. Under the maximised cooling rate scanning strategy, thermal gradients exhibit greater variations but generally remain lower than the conventional island printing approach. After printing the first 10 islands, the thermal gradients rapidly decrease, eventually reaching approximately 100 K/mm before completion. As indicated the maximised cooling rate strategy reduces thermal gradients, but it may introduce significant fluctuations during the process. The minimised temperature gradients strategy successfully reduces overall thermal gradients. Throughout the process, thermal gradients remain relatively low (consistently below 200 K/mm) and exhibit a gradual upward trend. Quantitative comparisons further confirm the distinct behaviour of the three scanning strategies. The average thermal gradient of the conventional island-printing case is approximately 243 K/mm, while the values for the

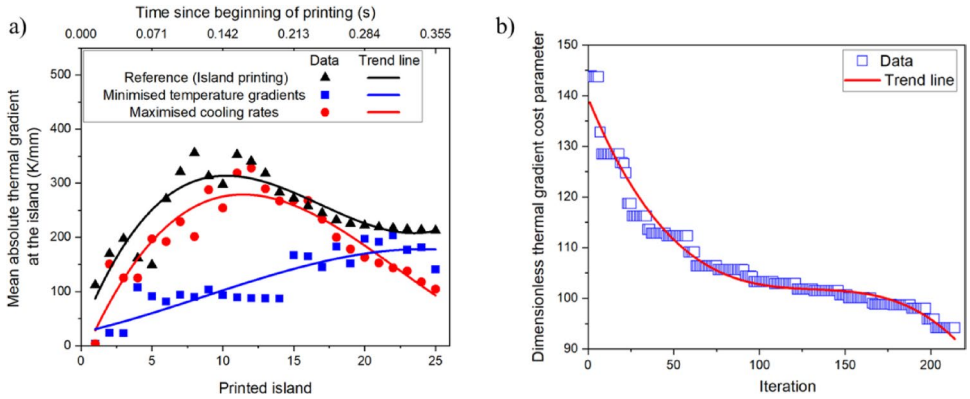

Fig. 2 **a** Mean absolute thermal gradient at the most recently printed island for different scanning strategies; **b** Evolution of the dimensionless thermal gradient cost parameter over iterations

maximised cooling rate and minimised temperature gradient strategies decrease by about 17% and 50%, respectively. In addition, the average thermal gradient for the line scanning case was approximately 4900 K/mm, which is about one order of magnitude higher than that of the island-printing strategies. This comparison is provided in the Supplementary Information (Fig. S3) to illustrate the pronounced thermal non-uniformity associated with continuous line scanning.

Figure 2b shows the dimensionless thermal gradient cost parameter evolution with increasing iterations. The dimensionless thermal gradient cost parameter decreases with iterations, reflecting the effectiveness of the optimisation process. Initially (0–50 iterations), the cost is high (>140). Between 50 and 150 iterations, it rapidly declines (~100), and after 150 iterations, it stabilises around 90. This suggests that the optimisation algorithm (genetic algorithm) successfully refines the scanning strategy, reducing thermal gradient costs. The convergence indicates an optimised strategy has been found where deep learning-based optimisation (GA+CNN) effectively adjusts scanning paths.

4.2 Crystallographic orientations and thermal history

EBSD maps and pole figures obtained from the fabricated samples are compared in Fig. 3a. All four samples exhibit fully face-centered cubic (FCC) phase. The line printing sample displays pronounced columnar grain structures with significant orientation clustering in the < 100 > direction which indicates strong texture formation. The three island printing samples show more uniform orientation distributions in pole figures, suggesting this printing method reduces the formation of texture. The conventional island printing sample shows non-uniform grain size distribution with larger grains in certain regions; this heterogeneity may lead to localised stress concentrations that affect mechanical properties [22, 23]. The minimised temperature gradients scanning strategy produced slightly larger grain sizes compared to conventional island printing without significantly oversized grains, indicating that moderate cooling rate (Fig. 2a) promoted more stable grain growth. The maximised cooling rates scanning strategy resulted in smaller grain sizes, demonstrating that rapid cooling inhibited heterogeneous nucleation and refined microstructures.

Figure 3b and c compare the evolution of temperature gradients and cooling rate of top-left corner of the sample for different island scanning strategies during the additive process. The top-left corner is corresponding to the 1st position of the sequence of conventional island printing, the 10th position for maximised cooling rates, and the 25th position for minimised temperature gradients-based printings, respectively. For conventional island printing, the temperature gradient is initially high (~700 K/mm) and gradually decreasing but maintaining within the 400–500 K/mm range throughout the process. In the maximised cooling rates scanning strategy, temperature gradients begin near 0 but rapidly increase after printing commences then gradually decrease during subsequent printing operations. This demonstrates that the rapid cooling strategy significantly reduces initial temperature gradients but causes certain regions to experience sudden thermal shock when new islands are printed. For minimised temperature gradients, the temperature gradient remains close to 0 throughout the printing process. It rises only during the final upper-left corner printing and reaches only 450 K/mm, lower than previous temperature gradients. This indicates that this strategy effectively reduces temperature gradient variations during printing, resulting in a more uniform temperature field. Regarding the cooling rate variations, all three scanning strategies initially exhibited negative cooling rates (heating) when printing reached specific points. Due to our assumptions about powder bed functions as an infinite heat sink, the two deep learning-derived scanning strategies displayed extremely high heating rates. However, the subsequent cooling rates aligned with expectations, where the maximised cooling rate strategy showed cooling at 8×10^3 K/s after heating, while the reference and maximised cooling rates strategies exhibited

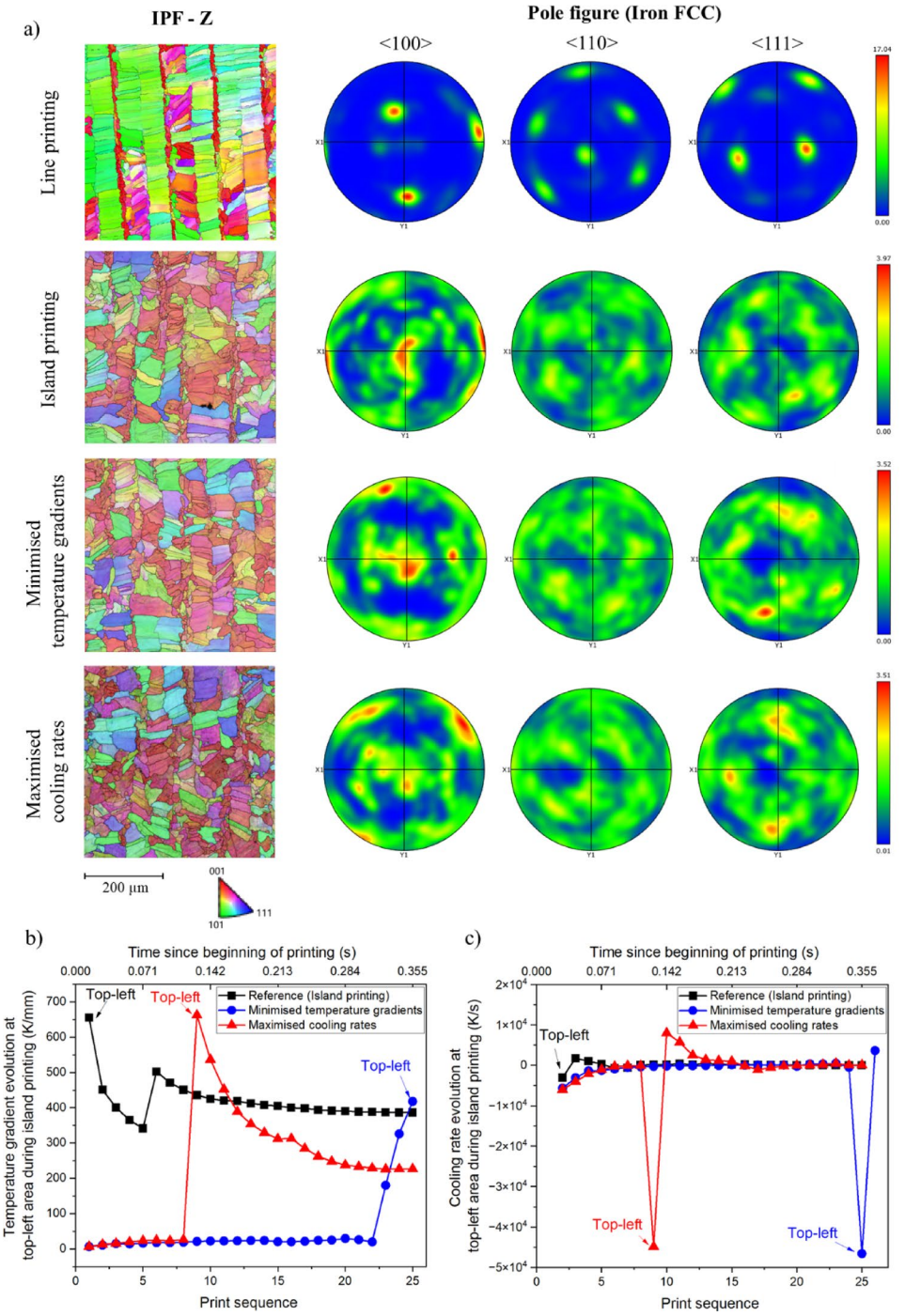

Fig. 3 **a** Representative EBSD (IPF-Z) maps and corresponding pole figures for different printing strategies; Evolution of **b** temperature gradients and **c** cooling rate for different island scanning strategies at top-left island location of island printing samples during the printing of one layer. The time the island is deposited is marked

only 1.7×10^3 K/s and 3.6×10^3 K/s, respectively. The peak local temperature gradient of the maximised cooling rates strategy changes by approximately + 1%, whereas that of the minimised temperature gradients strategy decreases by about 36% compared with the conventional island printing case. Regarding the peak cooling rate in Fig. 3c, the minimised temperature gradient and maximised cooling rate strategies exhibit approximately fourfold and twofold higher values, respectively, relative to the conventional island printing strategy. These quantitative results confirm that the CNN-GA optimisation framework provides effective and physically interpretable control of the spatiotemporal thermal conditions, which directly contribute to the refined and more uniform microstructures observed in the fabricated samples. Comparatively, the higher temperature gradients of conventional island printing result in non-uniform grain structures. Maximised cooling rates refine grain size, but local thermal plummet may induce greater local

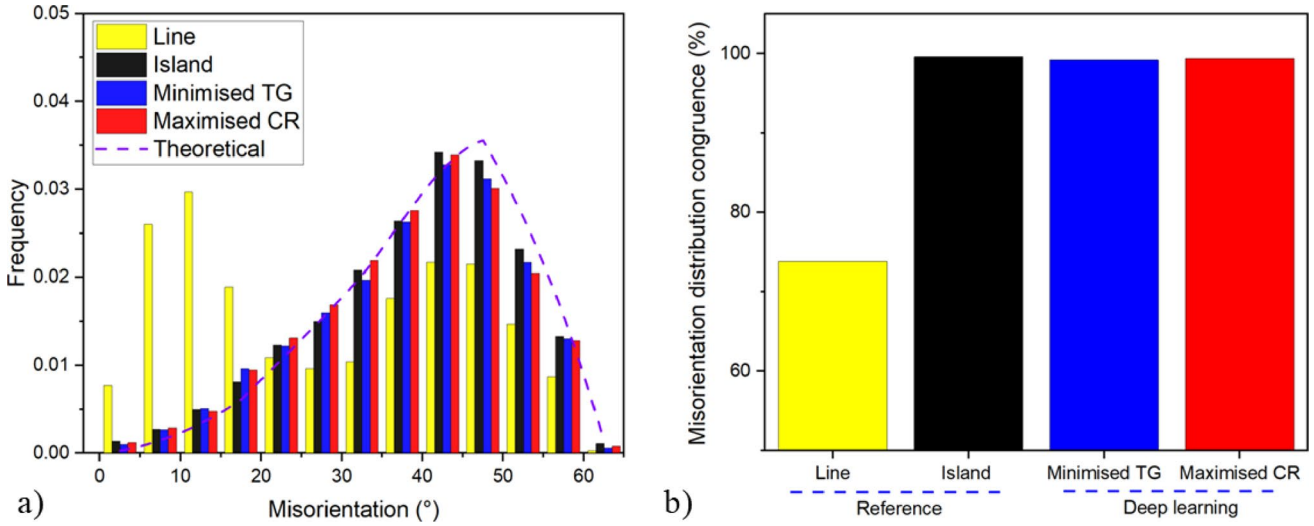

Fig. 4 **a** Misorientation angle distributions for all samples compared with the theoretical distribution and **b** corresponding misorientation distribution congruence values

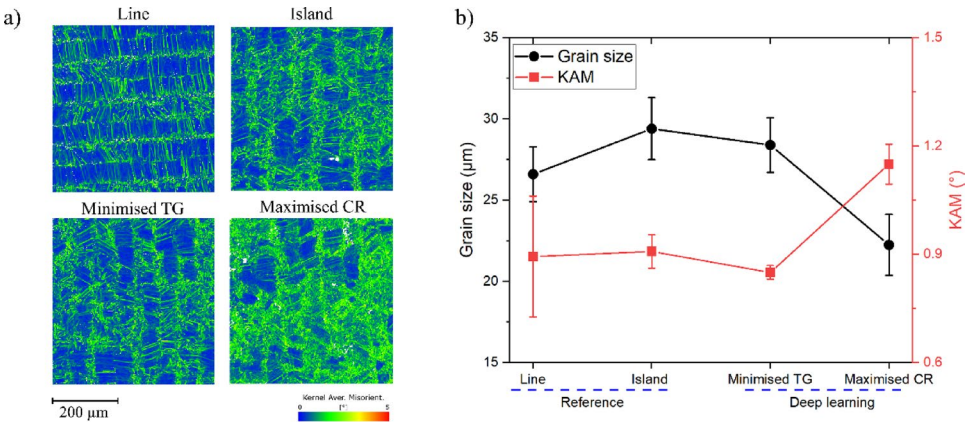

Fig. 5 **a** Representative kernel average misorientation (KAM) maps for different printing strategies; **b** Comparison of average grain size and KAM for line, island, minimised temperature gradient (TG) and maximised cooling rate (CR) approach

strain and stress. Minimised temperature gradients reduce heat accumulation with a moderate cooling rate, producing more uniform grains with reduced texture.

In addition, to further demonstrate that the island scanning strategy reduces crystallographic texture compared to the conventional line approach, Fig. 4 presents a quantitative comparison of misorientation angle distributions across different samples. As shown in Fig. 4a, the frequency distributions reveal distinct differences between the reference line sample and the island-based samples. The congruence analysis in Fig. 4b provides a quantitative measure of how closely each experimental distribution matches the theoretical random distribution. The reference line sample shows a congruence value of approximately 73%, indicating a higher degree of preferred texture. In contrast, the three island-based samples all achieve congruence values approaching 99%, indicating near-random crystallographic orientations with substantially reduced texture. This difference in congruence clearly demonstrates the advantage of the island scanning strategy in minimizing crystallographic texture.

4.3 Grain size and internal state

KAM maps for four different approaches are shown in Fig. 5a. All four approaches exhibit high KAM values at grain boundaries (compared to Fig. 3a). The KAM is a measure of local grain misorientation, with high KAM values indicating more local orientation variations with substantial plastic deformation and geometrically necessary dislocations (GNDs) accumulate regions. The conventional island printing shows slightly higher KAM distribution compared to line printing. The deep learning-based scanning strategies demonstrate distinct differences, with the minimised temperature gradient approach exhibiting overall lower KAM values. In contrast, the maximised cooling rate approach displays the most pronounced KAM distribution among all approaches, indicating that higher cooling rates lead to greater dislocation accumulation and localised strain.

Quantitative comparison of average grain size and KAM values obtained for different scanning strategies are presented in Fig. 5b (represent the average values obtained

from the five EBSD measurement regions shown in supplementary Fig. S2). As shown, conventional island printing exhibits larger grain sizes compared to line printing (29 vs. 26 μm), which may be attributed to batch-wise solidification resulting in slower cooling rates. The maximised cooling rates strategy contributes to grain size reduction as intended [41, 42], with measurements showing a decrease of 25% compared to conventional island printing (to approximately 22 μm). The minimised temperature gradients strategy produces grain sizes between those of conventional island printing and maximised cooling rates. This indicates that reducing temperature gradients aids grain refinement, though with limited effectiveness. KAM results reveal the lowest values (approximately 0.85°) for the minimised temperature gradients scanning strategy, indicating reduced local plastic strain and residual stress. In contrast, high cooling rates produce higher KAM values (1.15°) from abrupt temperature drops that lead to thermal stress accumulation. This is due to rapid solidification increases thermal stresses, promoting dislocation formation and accumulation, while minimising temperature gradients reduces this internal incompatibility.

The observed trends can be explained by well-established principles of solidification [43, 44]. Grain refinement achieved under the maximised cooling rate strategy follows the inverse relationship between grain size and nucleation undercooling, where higher cooling rates enhance nucleation density and shorten growth duration [45, 46]. In contrast, lowering the temperature gradient reduces thermal mismatches and the accumulation of geometrically necessary dislocations, leading to smaller KAM values and a more uniform internal strain/stress distribution [47]. Previous investigation have also reported that residual stress in LPBF components increases with the magnitude of thermal gradients, which supports this interpretation [8]. Variations in crystallographic texture can be further understood from differences in heat flow directionality and temperature gradient. The line scanning promotes competitive growth along the primary heat flow direction with a higher temperature gradient, producing a pronounced texture, whereas island based strategies create multidirectional heat flow and lower temperature gradient that disrupts preferential grain growth and weakens texture development [20]. These findings demonstrate that the CNN-GA based optimisation framework enables microstructural control through thermally driven and physically interpretable mechanisms.

5 Conclusive summary

The main findings of this study are summarised below:

i. The integrated CNN-GA framework effectively optimised island-scanning strategies by regulating the spatiotemporal temperature field during laser powder bed fusion. By predicting spatiotemporal temperature fields with the CNN and iteratively refining scanning sequences through the GA to achieve targeted regulation. The optimisation process exhibited clear convergence, with the dimensionless thermal gradient cost parameter stabilising around 90 after 150 iterations.
ii. The island scanning strategies significantly reduces texture formation compared to conventional line scanning due to lower temperature gradient.
iii. This thermal regulation and management approach demonstrated a reduction in temperature gradients and refinement of microstructure through controlled cooling rates, while lower KAM values observed under the minimised temperature-gradient strategy. Compared with conventional island printing, the maximised cooling rate strategy reduced average thermal gradients by 17%, and the minimised temperature gradient strategy by 50%. EBSD analysis confirmed that the maximised cooling rate strategy refined grain size by 25%, while the minimised temperature gradient strategy reduced average KAM values by 26%, indicating lower residual stress and local plastic strain.
iv. These results demonstrate that the deep learning-driven framework provides a physics-informed and computationally efficient route for microstructure control and residual-stress mitigation in metallic additive manufacturing that would otherwise require extensive and time-consuming trial-and-error iterations.

Supplementary Information The online version contains supplementary material available at https://doi.org/10.1007/s40964-025-01467-w.

Acknowledgements The authors acknowledge the UK Space Agency grant ST/Z00053X/1. EPSRC grants EP/R00661X/1, EP/S019367/1, EP/P025021/1, and EP/P025498/1 (Henry Royce Institute) are also acknowledged for enabling access to electron microscopy facilities.

Author contributions Fan Wu: Investigation, Formal analysis, Writing—original, Writing—review & editing, Methodology, Visualization. Clint Grohmann: Investigation, Formal analysis, Writing—review & editing, Methodology, Visualization. Feng Ji: Investigation, Writing—review & editing. Zhe Cai: Investigation. Lu Yang: Investigation, Writing— review & editing. Paulo Bartolo: Funding acquisition, Writing—review & editing. Wajira Mirihanage: Conceptualization, Funding acquisition, Supervision, Writing— review & editing. Fan Wu and Clint Grohmann contributed equally to this work.

Data availability The data that support the findings of this study are available from the corresponding author upon reasonable request.

Declarations

Conflict of interest No potential conflict of interest was reported by the author(s).

References

1. DebRoy T, Wei HL, Zuback JS, Mukherjee T, Elmer JW, Milewski JO, Beese AM, Wilson-Heid A, De A, Zhang W (2018) Additive manufacturing of metallic components – process, structure and properties. Prog Mater Sci 92:112–224
2. Wang YM, Voisin T, McKeown JT, Ye J, Calta NP, Li Z, Zeng Z, Zhang Y, Chen W, Roehling TT, Ott RT, Santala MK, Depond PJ, Matthews MJ, Hamza AV, Zhu T (2018) Additively manufactured hierarchical stainless steels with high strength and ductility. Nat Mater 17(1):63–71
3. Zhang W, Guo D, Wang L, Davies CM, Mirihanage W, Tong M, Harrison NM (2023) X-ray diffraction measurements and computational prediction of residual stress mitigation scanning strategies in powder bed fusion additive manufacturing. Addit Manuf 61:103275
4. Robinson J, Ashton I, Fox P, Jones E, Sutcliffe C (2018) Determination of the effect of scan strategy on residual stress in laser powder bed fusion additive manufacturing. Addit Manuf 23:13–24
5. Liu J, Wen P (2022) Metal vaporization and its influence during laser powder bed fusion process. Mater Design 215:110505
6. Chaudry MA, Mohr G, Hilgenberg K (2022) Experimental and numerical comparison of heat accumulation during laser powder bed fusion of 316L stainless steel. Progress Additive Manuf 7(5):1071–1083
7. Abd-Elaziem W, Elkatatny S, Abd-Elaziem A-E, Khedr M, Abd El-baky MA, Hassan MA, Abu-Okail M, Mohammed M, Järvenpää A, Allam T, Hamada A (2022) On the current research progress of metallic materials fabricated by laser powder bed fusion process: a review. J Mater Res Technol 20:681–707
8. Cheng B, Shrestha S, Chou K (2016) Stress and deformation evaluations of scanning strategy effect in selective laser melting. Addit Manuf 12:240–251
9. Salmi A, Atzeni E (2020) Residual stress analysis of thin AlSi10Mg parts produced by laser powder bed fusion. Virtual Phys Prototyp 15(1):49–61
10. Li F, Wang Z, Zeng X (2017) Microstructures and mechanical properties of Ti6Al4V alloy fabricated by multi-laser beam selective laser melting. Mater Lett 199:79–83
11. Li C, Lei H, Zhang Z, Zhang X, Zhou H, Wang P, Fang D (2020) Architecture design of periodic truss-lattice cells for additive manufacturing. Addit Manuf 34:101172
12. Jones P, Duncan S, Rayment T, Grant P (2007) Optimal robot path for minimizing thermal variations in a spray deposition process. 15(1):1–11
13. Chen Q, Taylor H, Takezawa A, Liang X, Jimenez X, Wicker R, To AC (2021) Island scanning pattern optimization for residual deformation mitigation in laser powder bed fusion via sequential inherent strain method and sensitivity analysis. Addit Manuf 46:102116
14. Zhang R, Strickland J, Hou X, Yang F, Li X, de Oliveira JA, Li J, Zhang S (2025) Rapid residual stress simulation and distortion mitigation in laser additive manufacturing through machine learning. Addit Manuf 102:104721
15. Liu Y, Li J, Xu K, Cheng T, Zhao D, Li W, Teng Q, Wei Q (2022) An optimized scanning strategy to mitigate excessive heat accumulation caused by short scanning lines in laser powder bed fusion process. Addit Manuf 60:103256
16. Thijs L, Kempen K, Kruth J-P, Van Humbeeck J (2013) Fine-structured aluminium products with controllable texture by selective laser melting of pre-alloyed AlSi10Mg powder. Acta Mater 61(5):1809–1819
17. Heeling T, Wegener K (2016) Computational investigation of synchronized multibeam strategies for the selective laser melting process. Physics Procedia 83:899–908
18. Masoomi M, Thompson SM, Shamsaei N (2017) Laser powder bed fusion of Ti-6Al-4V parts: thermal modeling and mechanical implications. Int J Mach Tools Manuf 118–119 73–90
19. Li C, Liu ZY, Fang XY, Guo YB (2018) On the simulation scalability of predicting residual stress and distortion in selective laser melting. J Manuf Sci Eng 140(4)
20. Nadammal N, Mishurova T, Fritsch T, Serrano-Munoz I, Kromm A, Haberland C, Portella PD, Bruno G (2021) Critical role of scan strategies on the development of microstructure, texture, and residual stresses during laser powder bed fusion additive manufacturing. Addit Manuf 38:101792
21. Evans R, Gockel J (2021) Modeling the effects of coordinated multi-beam additive manufacturing. Int J Adv Manuf Technol 115(4):1075–1087
22. Kruth J-P, Deckers J, Yasa E, Wauthlé R (2012) Assessing and comparing influencing factors of residual stresses in selective laser melting using a novel analysis method. Proc Institution Mech Eng Part B: J Eng Manuf 226(6):980–991
23. Lu Y, Wu S, Gan Y, Huang T, Yang C, Junjie L, Lin J (2015) Study on the microstructure, mechanical property and residual stress of SLM Inconel-718 alloy manufactured by differing Island scanning strategy. Opt Laser Technol 75:197–206
24. Mugwagwa L, Dimitrov D, Matope S, Yadroitsev I (2019) Evaluation of the impact of scanning strategies on residual stresses in selective laser melting. Int J Adv Manuf Technol 102(5):2441–2450
25. Kruth J-P, Badrossamay M, Yasa E, Deckers J, Thijs L, Van Humbeeck J (2010) Part and material properties in selective laser melting of metals, proceedings of the 16th international symposium on electromachining (ISEM XVI), Shanghai Jiao Tong Univ Press, pp. 3–14
26. Qiu C, Adkins NJE, Attallah MM (2013) Microstructure and tensile properties of selectively laser-melted and of hiped laser-melted Ti–6Al–4V. Mater Sci Engineering: A 578:230–239
27. Qin M, Ding J, Qu S, Song X, Wang CCL, Liao W-H (2024) Deep reinforcement learning based toolpath generation for thermal uniformity in laser powder bed fusion process. Addit Manuf 79:103937
28. Lapointe S, Guss G, Reese Z, Strantza M, Matthews MJ, Druzgalski CL (2022) Photodiode-based machine learning for optimization of laser powder bed fusion parameters in complex geometries. Addit Manuf 53:102687

29. Ren K, Chew Y, Zhang YF, Fuh JYH, Bi GJ (2020) Thermal field prediction for laser scanning paths in laser aided additive manufacturing by physics-based machine learning. Comput Methods Appl Mech Eng 362:112734
30. Dharmawan AG, Xiong Y, Foong S, Soh GS, Model-Based A (2020) Reinforcement learning and correction framework for process control of robotic wire arc additive manufacturing, 2020 IEEE International Conference on Robotics and Automation (ICRA), pp. 4030–4036
31. Mondal S, Gwynn D, Ray A, Basak A (2020) Investigation of melt pool geometry control in additive manufacturing using hybrid modeling, Metals
32. Wang C, Tan XP, Tor SB, Lim CS (2020) Machine learning in additive manufacturing: state-of-the-art and perspectives. Addit Manuf 36:101538
33. Sing SL, Kuo CN, Shih CT, Ho CC, Chua CK (2021) Perspectives of using machine learning in laser powder bed fusion for metal additive manufacturing. Virtual Phys Prototyp 16(3):372–386
34. Taylor B Methodus incrementorum directa & inversa, Inny1717
35. Pichler P, Simonds BJ, Sowards JW, Pottlacher G (2020) Measurements of thermophysical properties of solid and liquid NIST SRM 316L stainless steel. J Mater Sci 55(9):4081–4093
36. Dantzig J, Rappaz M, Solidification EPFL, Press (2009) Lausanne, Switzerland 249–285
37. Simonyan K, Zisserman AJC (2014) Very deep convolutional networks for large-scale image recognition, abs/1409.1556
38. Kingma D, Ba J (2014) Adam: A method for stochastic optimization, international conference on learning representations
39. He K, Zhang X, Ren S, Sun J (2016) Deep residual learning for image recognition, 2016 IEEE Conference on Computer Vision and Pattern Recognition (CVPR), pp. 770–778
40. Chollet F (2015) Keras. GitHub. Available at: https://github.com/fchollet/keras
41. Liang G, Ali Y, You G, Zhang M-X (2018) Effect of cooling rate on grain refinement of cast aluminium alloys. Materialia 3:113–121
42. StJohn DH, Qian M, Easton MA, Cao P (2011) The interdependence theory: the relationship between grain formation and nucleant selection. Acta Mater 59(12):4907–4921
43. Zhang W, Cai Z, Wu F, Mirihanage W, Lupoi R (2025) Grain morphology selection during metal additive manufacturing with powder sheets (MAPS). Mater Today Commun 48:113345
44. Ali Y, Qiu D, Jiang B, Pan F, Zhang M-X (2015) Current research progress in grain refinement of cast magnesium alloys: a review Article. J Alloys Compd 619:639–651
45. Liu J, Song Y, Chen C, Wang X, Li H, Zhou Ca, Wang J, Guo K, Sun J (2020) Effect of scanning speed on the microstructure and mechanical behavior of 316L stainless steel fabricated by selective laser melting. Mater Design 186:108355
46. Jang K-N, Kim T-K, Kim K-T (2019) The effect of cooling rates on carbide precipitate and microstructure of 9CR-1MO oxide dispersion strengthened(ODS) steel. Nuclear Eng Technol 51(1):249–256
47. Leicht A, Rashidi M, Klement U, Hryha E (2020) Effect of process parameters on the microstructure, tensile strength and productivity of 316L parts produced by laser powder bed fusion. Mater Charact 159:110016